Fabrication and hydrogen permeation resistance of dense CrN coatings

Liangliang Liu [a,c,d,1], Qingdong Ruan [a,c,d,1], Shu Xiao [a,b,c,d,*], Xinyu Meng [b], Chao Huang [a,c,d], Yuzheng Wu [a,c,d], Ricky K.Y. Fu [a,c,d], Paul K. Chu [a,c,d,*]

[a] Department of Physics, City University of Hong Kong, Tat Chee Avenue, Kowloon, Hong Kong, China
[b] Institute of Safety Science & Engineering, South China University of Technology, Guangzhou 510641, China
[c] Department of Materials Science and Engineering, City University of Hong Kong, Tat Chee Avenue, Kowloon, Hong Kong, China
[d] Department of Biomedical Engineering, City University of Hong Kong, Tat Chee Avenue, Kowloon, Hong Kong, China

ABSTRACT

Hydrogen embrittlement has become a hot research topic due to the rapid development of hydrogen energy and coating technology is regarded as the most efficient method to mitigate hydrogen embrittlement. However, the grain gaps in coatings frequently serve as paths for hydrogen permeation thus decreasing the protecting effects. In this work, ion bombardment is performed during magnetron sputtering deposition of dense CrN coatings to decrease the formation of grain gaps. The compactness of the CrN coatings is improved by disrupting the growth of grains using energetic ion bombardment. Hydrogen permeation tests reveal that the apparent hydrogen diffusion coefficient and hydrogen permeability of the dense CrN coating 52.6 and 24.1 times less than those of the unprotected substrate. The tensile test also reveals excellent hydrogen embrittlement resistance compared to the X70 substrate and conventional coatings.

1. Introduction

Hydrogen energy is drawing enormous attention because of its high calorific value, sustainability, and environmental friendliness [1]. However, owing to hydrogen embrittlement (*HE*) in steels in the hydrogen atmosphere, catastrophic failure of hydrogen storage devices and facilities can occur during storage or transportation [2]. Therefore, it is imperative to improve the hydrogen embrittlement resistance of steels.

The conventional strategy is to use steels with better hydrogen embrittlement and cracking resistance such as X70 [3,4] in which the interlocked polygonal ferrite structure abates crack propagation. However, this method cannot circumvent the problem totally and hydrogen barriers have been proposed to reduce the damage [5]. In this respect, coatings are commonly deposited to isolate the steel surface from hydrogen in order to offer better resistance to hydrogen permeation. Ceramic coatings such as TiN [6], TiC [7], CrN [8], Al_2O_3 [9], and Si_3N_4 [10] have been proposed because of the excellent mechanical properties and inertness, especially in harsh environments. Those coatings could enhance the hydrogen permeation resistance to more than 100 times depended on the types of substrates and coatings (materials, thickness

and compactness of coatings) [11]. Those coatings are commonly deposited by physical vapor deposition (PVD) techniques such as magnetron sputtering (MS) and arc ion plating as well as chemical vapor deposition (CVD). In particular, MS is often used to fabricate these coatings because the low deposition temperature does not alter the phase and structure of the steel substrate significantly [12,13]. Besides, the technique is droplet free and can produce coatings with relatively few pores and holes compared to other methods such as arc ion plating, laser cladding, plasma spraying, and so on [14,15]. However, Li et al. have found the hydrogen permeation resistance of Al_2O_3 coatings is not enhanced when the coating thickness is increased from 200 nm to 1600 nm [16] because of the formation of grain gaps [17,18] that serve as channels for hydrogen permeation and drastically worsen the protection effects. Therefore, dense coatings without or with few grain gaps are preferred. Although different types of coatings have been prepared by varying the deposition parameters such as the plasma density, substrate temperature, and bias voltage [19–21], grain gaps cannot be avoided. According to the film growth mechanism [22,23], formation of grain gaps is negligible in the beginning of deposition due to the creation of nanograins. However, with increasing thickness or deposition time, the grain size increases gradually lead to an uneven and rough surface which

limits atom diffusion and promotes the formation of grain gaps [24]. However, during PVD, energetic ion bombardment is often used to improve the adhesion [25] and disrupt grain growth [26]. If ion bombardment is performed before the grains are large enough to form grain gaps, the coating compactness and hydrogen permeation resistance can be enhanced.

In this work, dense CrN coatings are prepared by MS and ion bombardment to improve the hydrogen resistance. Grain gaps are reduced significantly and even disappear after periodic ion bombardment. The chemical inertness and hydrogen permeation resistance are improved at the same time as manifested by a smaller hydrogen diffusion coefficient and better hydrogen embrittlement resistance.

2. Experimental details

Double-side polished X70 steel (50 mm × 30 mm × 1 mm) and silicon samples were used as the substrates. They were ultrasonically cleaned in acetone and ethanol for 20 min each before deposition. Deposition was carried out on the multi-functional plasma immersion ion implantation and deposition instrument with a 600 mm diameter and 1 m high vacuum chamber manufactured by Plasma Technology Ltd. (Hong Kong). The CrN coating was deposited by MS and ion bombardment was conducted using the filtered cathode vacuum arc (FCVA). The schematic diagram of the system is depicted in Fig. 1. After evacuating to a base pressure of 3×10^{-3} Pa and heating to 200 °C, the substrate was cleaned by an Ar plasma for 20 min generated by a linear anode layer ion source (10.0×48.0 cm^2) at a bias of -1200 V (40 kHz, 75% duty cycle). The Ar (99.999%) flow rate and pressure were 50 sccm and 0.6 Pa, respectively. The CrN coatings were deposited using a 99.9% pure Cr target (10.0×48.0 cm^2) in the Ar & N$_2$ (99.999%) environment. The MS power supply was operated at a power of 2 kW, frequency of 40 kHz, and duty cycle of 20%. The Ar and N$_2$ flow rates were 50 sccm and 20 sccm, respectively, and the pressure was 0.7 Pa. Before CrN deposition, a Cr/CrN$_x$ interlayer was deposited by gradually increasing the N$_2$ flow rate from 0 sccm to 20 sccm in 5 min. The conical Cr target in FCVA had upper and base diameters of 50 and 70 mm, respectively. The cathode current was 40 A to produce Cr ions for ion bombardment. In this way, ALIS, MS, and FCVA were carried out all the time during the process. After deposition of CrN with a specific thickness by MS, the sample was rotated in front of FCVA for ion bombardment at a bias of -400 V. The MS and FCVA procedures were repeated to produce the full layer and the important instrumental parameters are listed in Table 1.

The thickness and morphology of the coatings were examined by field-emission scanning electron microscopy (FE-SEM, ZEISIS SUPRA@55). X-ray diffraction (Bruker, D8 discover) was employed to determine the phase and crystallinity of the coatings at a scanning step of 0.02° using Cu K$_\alpha$ X-ray (1.5406 Å). The corrosion resistance was

evaluated on an electrochemical workstation (Zahner Zennium, USA) based on the three-electrode technique in a 3.5% NaCl solution. Platinum and Hg/Hg$_2$Cl$_2$ were the counter and reference electrodes, respectively and the exposed sample surface area was 0.25 cm^2. After immersion in the solution for 30 min, potentiodynamic polarization was conducted at a scanning rate of 1 mV·s^{-1} from -1.5 V to $+1.0$ V. Electrochemical impedance spectra (EIS) were acquired with a sinusoidal potential of 5 mV and frequency range between 100 kHz and 100 mHz. The EIS data was fitted by the Z-view 2 software and the relative error of fitting was less than 5% with the chi-square value (χ^2) ranging between 10^{-4}– 10^{-5} for the accuracy.

The electrochemical hydrogen permeation test was carried out using the Devanathan-Stachurski (D-S) cell [27] as shown in Fig. 2, composed of the cathode (hydrogen charging) and anode (hydrogen detection) with a platinum plate as the counter electrode, saturated calomel electrode (SCE) as the reference electrode, and sample as the working electrode. The cathode cell was filled with a solution of 0.2 mol/L NaOH and 3 g/L NH$_4$SCN and the anode cell was filled with 0.2 mol/L NaOH. Before the test, the background current was reduced to less than 0.1 μA/cm^2 by applying a constant potential of 200 mV (vs. SCE) to the anodic cell and then a constant current of -12 mA/cm^2 was applied to the cathode to start the test. The hydrogen was produced in the cathode cell and permeated through the coating-substrate to the anode, where it was detected. The i indicts the current detected in the anode cell due to the oxidation of hydrogen. Therefore, it could represent the permeated hydrogen through the sample. i_p^∞ indicts the steady anode current. According to Devanathan [27], the time lag (t_{lag}) corresponds to the point at which $i = 0.63i_p^\infty$ in the hydrogen permeation current curve. t_b is the time used for the hydrogen to pass through the sample which is found by extrapolating the linear portion of the initial hydrogen permeation current transient to $i = 0$. t_r is the rise time constant. The t_b, t_{lag} and t_r could be calculated according to the previous works [27,28]. The apparent diffusion coefficient of hydrogen (D_{app}) and permeability (J) could be calculated by Eqs. (1) and (2) [29,30].

$$D_{app} = \frac{L^2}{15.3t_b} \tag{1}$$

$$J = \frac{i_p^\infty \times L}{F} \tag{2}$$

where D_{app} (the apparent diffusion coefficient) is the hydrogen diffusion quality in 1 cm^2 per second at unit concentration gradient, J is hydrogen permeation rate in the materials, the L is the thickness of the sample in cm, t_b is the breakthrough time (s), i_p^∞ is the steady-state current density (μA/cm^2), and F = 96,485C/mol (Faraday constant). According to their definitions, a longer t_b, smaller i, smaller D_{app} and smaller J could reflect better hydrogen permeation resistance. The slow strain rate test (SSRT) was employed to evaluate the resistance to hydrogen embrittlement (HE) [31]. The hydrogen-charged samples were pre-charged electrochemically at 50 mA/cm^2 for 24 h before SSRT. After hydrogen charging, the test was carried out immediately to avoid thermal desorption and escape of hydrogen. The strain rate was 5.5×10^{-5}/s. With the exception of the exposed area on the coating side, the rest of the sample was covered by sealing mud, so that hydrogen charging only occurred on the measured region.

3. Results and discussion

The cross-sectional morphology of the coatings prepared by MS only and MS with ion bombardment is displayed in Fig. 3. Samples S6-1, S4-1, and S2-1 are deposited for 6 min, 4 min, and 2 min accompanied by ion bombardment in each cycle. The coating thickness is about 3.3 μm and the Cr/CrN$_x$ interlayer is 0.8 μm thick. The coating deposited by MS in Fig. 3(a) shows a dense structure near the substrate. With increasing thickness, the columnar structure becomes more obvious and clear grain
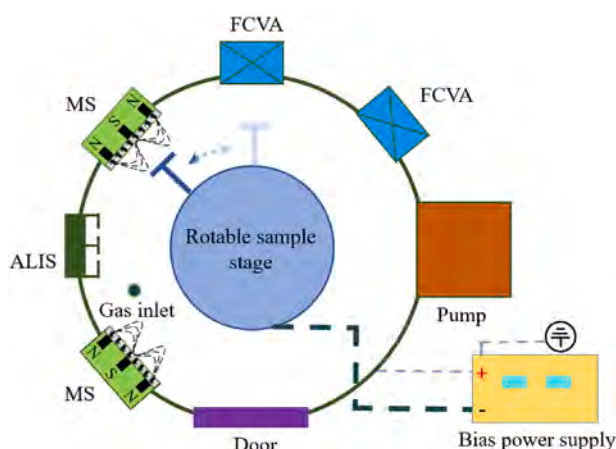

Fig. 1. Schematic diagram of the vacuum system.

Table 1
Important deposition parameters.

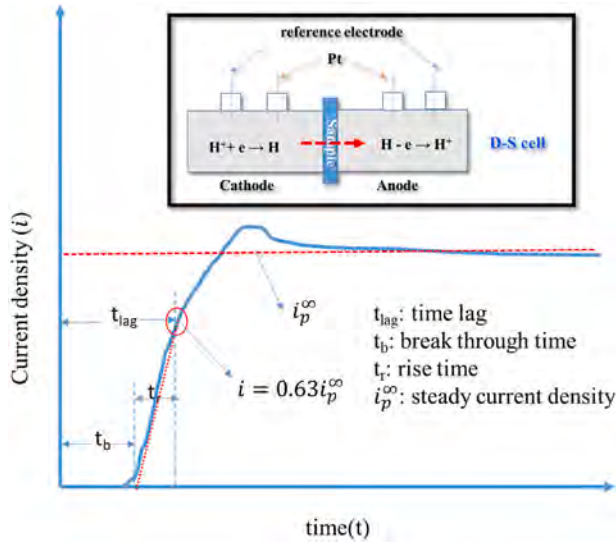| Sample name	MS layer			FCVA interrupting layer			Cycles
	Time (min)	Thickness (nm)	Bias (V)	Time (min)	Thickness (nm)	Bias (V)	
MS	45	2500	−100	–	–	–	–
S6-1	6	300	−100	1	10	−400	8
S4-1	4	200	−100	1	10	−400	11
S2-1	2	100	−100	1	10	−400	22

Fig. 2. The working principle of the D-S cell and the illustration of electrochemical hydrogen permeation current curves.

gaps are observed from the MS coatings. Owing to the low ionization rate, most of the particles are neutral and not accelerated towards the substrate thereby limiting solid-state diffusion giving rise to the sparse

and columnar structure [24]. No obvious sublayer interface is observed from S6-1 in the middle 1.2 μm corresponding to the first 4 cycles. This stems from the formation of the sparse structure after deposition of the interlayer layer in the early cycles. When the ions produced by FCVA arrive at the surface, they tend to diffuse to the gaps but do not disrupt film growth and therefore, no apparent disruption is observed in the first few cycles. However, grain gaps become unclear because of filling and so the coating compactness increases compared to the MS only sample. With increasing ion bombardment cycles, the structure becomes denser and show clear interfaces in the horizontal direction corresponding to the ion bombardment period. By further increasing the ion bombardment cycles, the coating becomes denser and no obvious grain boundary can be observed from S2-1 which is expected to reduce hydrogen permeation.

Fig. 4 presents the surface morphology of the sample shown in Fig. 4 (a) revealing a loose structure with a stack of flakes. Many distinctive grain gaps are distributed in the coatings due to insufficient diffusion of the particles. These grain gaps decrease the coating compactness and provide paths for hydrogen permeation. Samples S6-1 and S4-1 in Fig. 4 (b-c) exhibit a similar morphology as the MS sample. However, the flake size decreases with ion bombardment cycles resulting in smaller grain gaps and larger coating compactness. By further decreasing the disrupting period to 100 nm (S2-1), grain boundaries become indistinguishable and the coating compactness is larger due to the refined grain size as shown in Fig. 4(d).

The structure and crystallinity of the coatings are determined by XRD as shown in Fig. 5. All the samples are polycrystalline having the face-
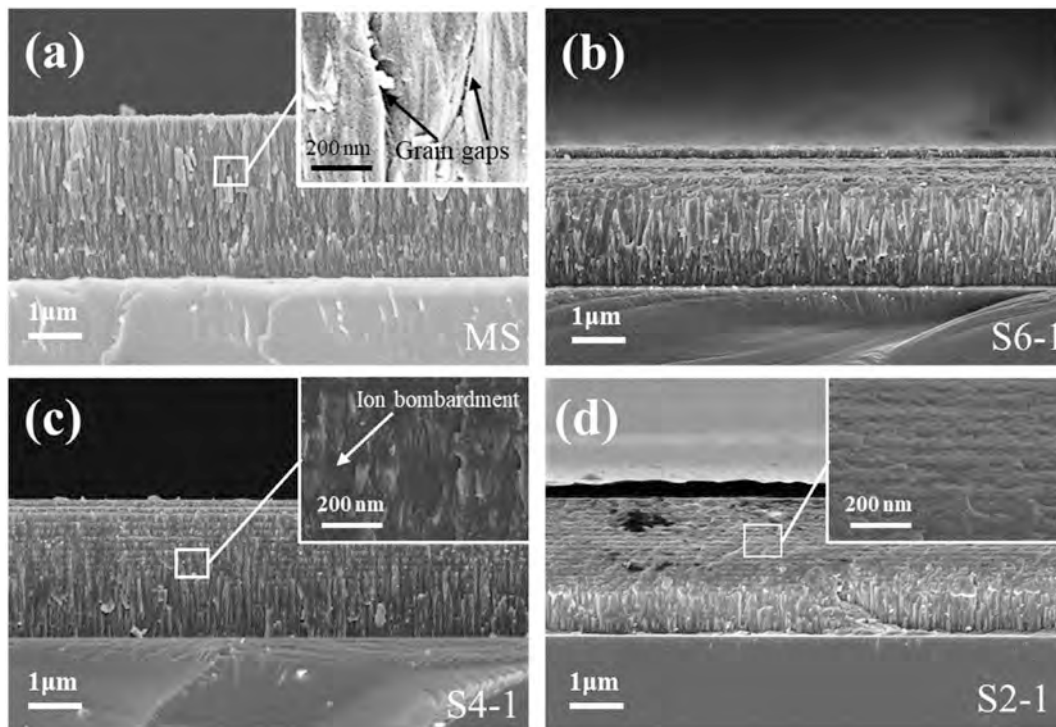

Fig. 3. Cross-sectional morphology of the coatings: (a) MS, (b) S6-1, (c) S4-1, and (d) S2-1.
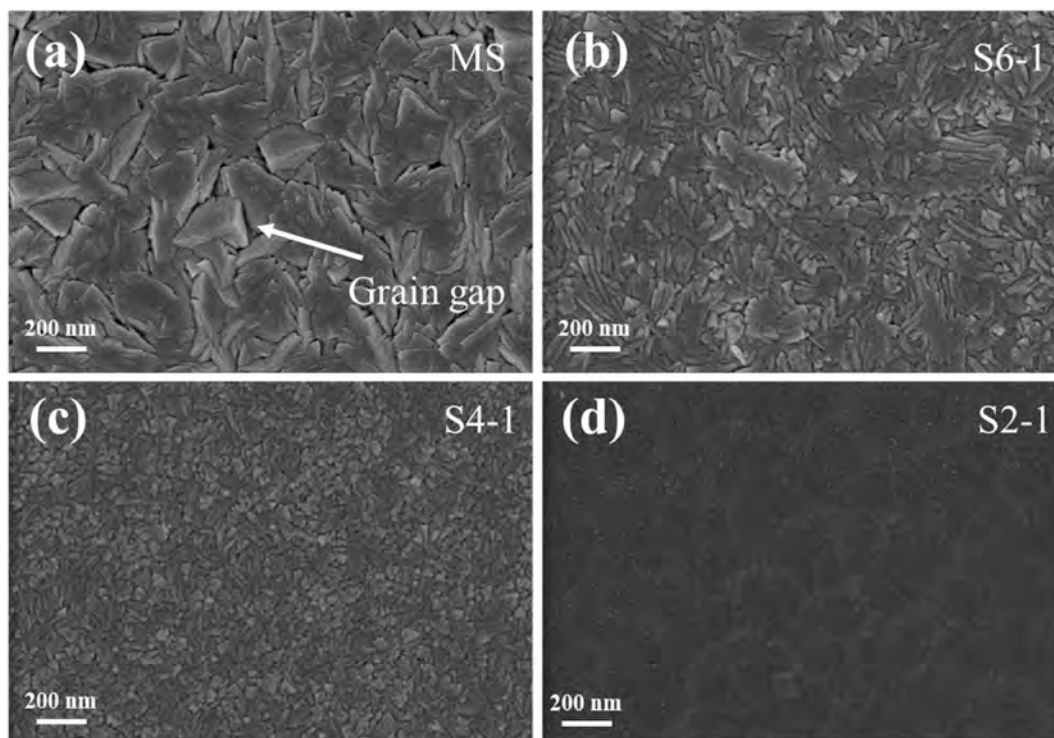
Fig. 4. Surface morphology of the samples: (a) MS, (b) S6-1, (c) S4-1, and (d) S2-1.

centered cubic (fcc) structure (PDF#11-0065) and (200) preferred orientation. However, there are some differences among the samples. The (200) peak broadens with ion bombardment due to refined grains as shown in Figs. 3–4 [32] and the refined grains provide sites for growth in other orientations. As a result, the (111) peak intensity of S4-1 and S2-1 is larger after ion bombardment.

Corrosion is the primary source of hydrogen in common applications of steels and the corrosion resistance affects the hydrogen permeation capability. As shown by the potentiodynamic polarization results in Fig. 6, the corrosion potential (E_{corr}) and corrosion current (I_{corr}) derived by Tafel extrapolation from the linear cathodic polarization region are obtained and listed in Table 2. The samples with disrupted layers have higher E_{corr} and lower I_{corr} than the MS sample. In particular, S2-1 has the best corrosion resistance as manifested by the largest E_{corr} and smallest I_{corr} of −0.364 V and 1.51 μA/cm^2, respectively.

The electrochemical impedance spectra in Fig. 7(a) discloses two-

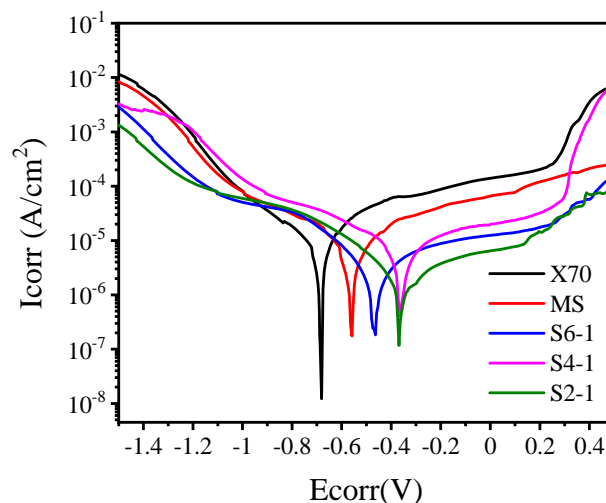**Fig. 6.** Potentiodynamic polarization results of the coatings.

Table 2
E_{corr} and I_{corr} of different samples.

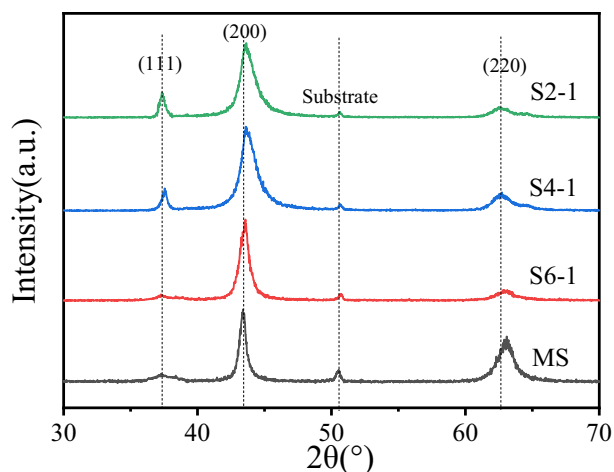|	X70	MS	S6-1	S4-1	S2-1
E_{corr} (V)	−0.684	−0.5597	−0.462	−0.363	−0.364
I_{corr} (μA/cm^2)	10.10	6.32	2.06	3.61	1.51

time constants which are better resolved for S4-1 and S2-1. The impedances of S4-1 and S2-1 are also larger as shown in Fig. 7(b) and the equivalent circuit in Fig. 7(d) is employed to model the EIS data. The equivalent circuit consists of the R_s, R_{pore}, R_{ct}, constant phase elements of *CPE1* and *CPE2* [33,34]. R_s represents the solution resistance of the electrolyte between the working electrode and reference electrode. R_{pore} represents the impedance for electrolyte in the pores and defects of the

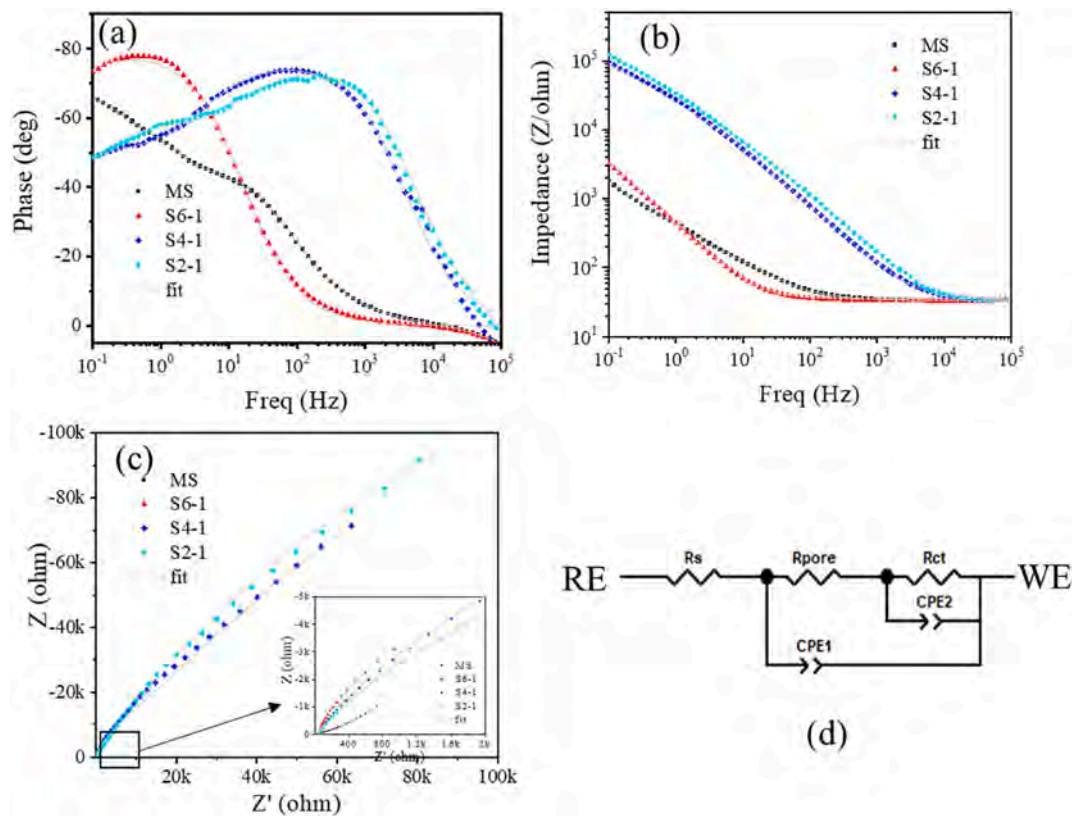**Fig. 5.** XRD patterns of the samples.

Fig. 7. Electrochemical impedance spectra: (a) Phase angle, (b) impedance, (c) Nyquist plots, and (d) equivalent circuits.

coating, which reflects the corrosion barrier effect of the coating. C_{coat} stand for the capacitance of the coating. The R_{ct} is the charge transfer resistance of the electrolyte/substrate interface, which can reflect the corrosion rate of the substrate. C_{pore} is used to evaluate the capacitance of defects in the coatings. CPE is generally necessary for porous PVD coatings because of deviation from the ideal capacitor to the non-ideal one because of surface roughness and inhomogeneity. The deviation from the perfect capacitor can be demonstrated by the parameter n which varies between 0 (pure resistance) to 1 (pure capacitance). According to the fitted data in Table 3, R_s varies from 33.63 to 35.66 $\Omega \cdot cm^2$ among the samples. Compared to the MS sample, the ion bombarded samples show higher R_{pore} and smaller C_{coat}, indicating that there are less defects in the coatings. Besides, penetration of the corrosive solution to the substrate is blocked as shown the larger R_{ct} and smaller C_{pore} arising from film densification. These results disclose that the corrosion resistance is improved with the aid of ion bombardment.

The hydrogen permeation results are displayed in Fig. 8(a). The t_b could reflect the time used for hydrogen passing through the coating-substrate. The current density (i) represents the permeation rate of the hydrogen. Therefore, longer t_b and lower i indicate better hydrogen permeation resistance. Hydrogen attacks the bare X70 substrate quickly. Thus, the equilibrium current is high and continues to increase during the test indicating poor hydrogen permeation resistance. MS and S6-1

show slightly shorter t_b and higher i. In comparison, the t_b are longer and i are smaller for S4-1 and S2-1 reflecting better hydrogen permeation resistance. Since the corrosion resistance of X70 is very poor, surface reaction of the X70 substrate occurs as it was exposed in alkaline solution. Therefore, it is hard to reach a steady permeation current for X70, MS and S6-1 even after more than 14 h test. In order to quantitatively calculate the D_{app} and J, the current when the time is 40,000 s ($i_{t=40,000s}$) was chosen as the i_p^∞. Although it might be imprecise, this operation would not affect the main conclusion because the i value is ranked as X70 > MS > S6-1 > S4-1 > S2-1 during most period of the test. The calculated results are presented in Table 4. The D_{app} and J of X70 are 5.94×10^{-6} cm^2/s and 2.85×10^{-5} mol·cm^{-1}·s^{-1}, respectively. Hydrogen permeation diminishes gradually with ion bombardment as verified by smaller D_{app} and J. The D_{app} and J of S2-1 are 1.13×10^{-7} cm^2/s and 1.14×10^{-6} mol·cm^{-1}·s^{-1}, respectively, which are 52.6 and 24.1 times less than those of the substrate as shown in Fig. 8(b).

Fig. 9 presents the strain-stress curves of the substrate and coated samples after electrochemical hydrogen charging. The mechanical properties and deformation characteristics are shown in Table 5. The uncharged X70 substrate show high yield strength, fracture strength and elongation of 612 MPa, 685 MPa and 18.1%, respectively. Due to the hydrogen embrittlement, the hydrogen charged X70 substrate has lower yield strength and fracture strength of 571 MPa and 637 MPa,

Table 3
Electrochemical parameters obtained by equivalent circuit simulation.

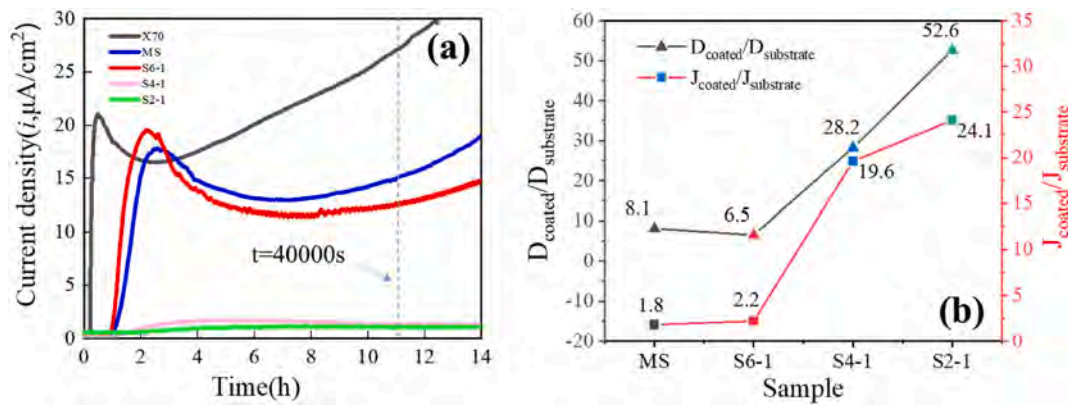|	Rs	Rpore	CPE1		Rct	CPE2		χ^2
	($\Omega \cdot cm^2$)	($\Omega \cdot cm^2$)	Ccoat-T ($\Omega^{-1} \cdot s^n \cdot cm^{-2}$)	CPE1-P	($\Omega \cdot cm^2$)	Cpore-T ($\Omega^{-1} \cdot s^n \cdot cm^{-2}$)	CPE2-P	
MS	33.63	107	6.22×10^{-4}	0.60923	10,881	1.19×10^{-3}	0.64230	5.156×10^{-5}
S6-1	35.66	29,633	4.42×10^{-4}	0.89602	29,971	4.52×10^{-4}	0.87961	7.254×10^{-5}
S4-1	33.81	28,177	4.97×10^{-6}	0.86146	450,000	1.11×10^{-5}	0.63898	2.391×10^{-4}
S2-1	35.16	34,638	3.37×10^{-6}	0.86248	443,780	6.78×10^{-6}	0.63599	3.472×10^{-4}

Fig. 8. (a) Electrochemical hydrogen permeation curves of the samples; (b) the improvement of D_{app} and J compared with the uncoated substrate.

Table 4
Hydrogen permeation parameters of the different samples.

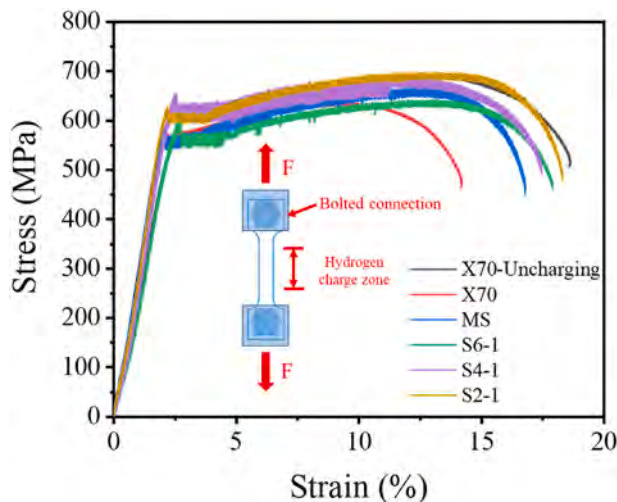| Sample	t_b/s	D_{app}/cm^2·s^{-1}	$I_{t=40,000s}$/µA·cm^{-1}	J/mol·cm^{-1}·s^{-1}
X70	110	5.94×10^{-6}	27.5	2.85×10^{-5}
MS	890	7.34×10^{-7}	15.1	1.56×10^{-5}
S6-1	720	9.08×10^{-7}	12.7	1.32×10^{-5}
S4-1	3100	2.11×10^{-7}	1.4	1.45×10^{-6}
S2-1	5790	1.13×10^{-7}	1.1	1.14×10^{-6}

Fig. 9. Strain-stress curves after electrochemical hydrogen charging.

Table 5
Mechanical properties and deformation characteristics.

Sample	Yield strength/MPa	Fracture strength/MPa	Elongation of hydrogen charged area/%
X70-uncharging	612	685	18.1
X70	571	637	13.8
MS	584	664	15.4
S6-1	600	632	16.7
S4-1	598	680	17.1
S2-1	609	682	17.6

respectively. Besides, elongation of the hydrogen charged area is limited to 13.8%. The MS sample also exhibit significant decrease in the yield strength, fracture strength, and elongation, revealing poor hydrogen blocking effects due to the significant grain gaps. On the contrary, after

ion bombardment, the coating structures of S2-1 become denser dramatically which could block the permeation of hydrogen, thus possessing the high fracture strength of about 680 MPa and elongation of 17.6%, which is close to the uncharged substrate.

The tensile fracture morphology is examined and shown in Fig. 10. After the extended test, flat dissociative fracture characteristics are observed indicative of brittle fracture. This phenomenon confirms irreversible hydrogen embrittlement which compromises the mechanical properties. The coated samples have the typical dimple morphology and the dimple size is larger with ion bombardment suggesting better plasticity. The dense coatings produced by ion bombardment alleviate hydrogen embrittlement of the substrate consistent with the hydrogen permeation and tensile results.

The mechanism of the hydrogen permeation resistance of the conventional and dense CrN coatings is illustrated in Fig. 11. The MS coating has a sparse structure with many grain gaps which can reach 10 nm and these gaps form easy paths for hydrogen to traverse to the substrate. On the other hand, the dense CrN coating produced by ion bombardment does not show obvious grain gaps and therefore, the hydrogen permeation mechanism is different from that of conventional MS coatings. The grain boundaries and atom interstice are generally larger than the size of the hydrogen atom thereby enabling hydrogen to permeate easily, but the CrN coatings offer much better hydrogen permeation resistance due to the dense structure and absence of grain gaps.

4. Conclusion

Coatings can block hydrogen permeation and mitigate hydrogen embrittlement in the steel substrate. However, grain gaps formed during coating growth decrease the protecting effects. In this work, energetic ion bombardment is performed in conjunction with magnetron sputtering to restrain grain growth and abate the formation of grain gaps. By means of periodic ion bombardment during magnetron sputtering, grain gaps are reduced and the coating compactness increases significantly. The hydrogen permeation test shows that the dense CrN coating decreases the apparent hydrogen diffusion coefficient and hydrogen permeability to 1.13×10^{-7} cm^2/s and 1.14×10^{-6} mol·cm^{-1}·s^{-1}, which are about 52.6 and 24.1 times less than those of the unprotected substrate. The tensile test also reveals better prevention of hydrogen embrittlement suggesting large application potential of the materials and methodology.

CRediT authorship contribution statement

L.L. Liu and **Q.D. Ruan**: Conceptualization, Methodology, Writing – original draft. **X. Shu, R.K.Y. Fu, P.K Chu**: Resource, Provision, Writing – review & editing. **X.Y. Meng, C. Huang**, and **Y.Z. Wu**: Analysis, **P.K.**
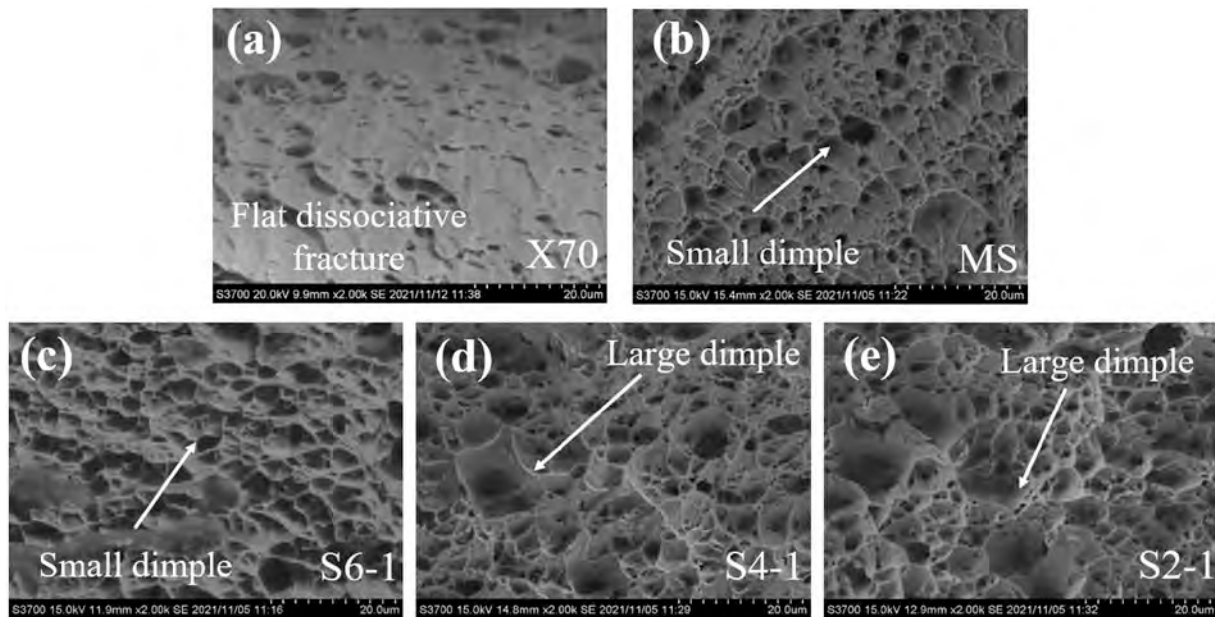
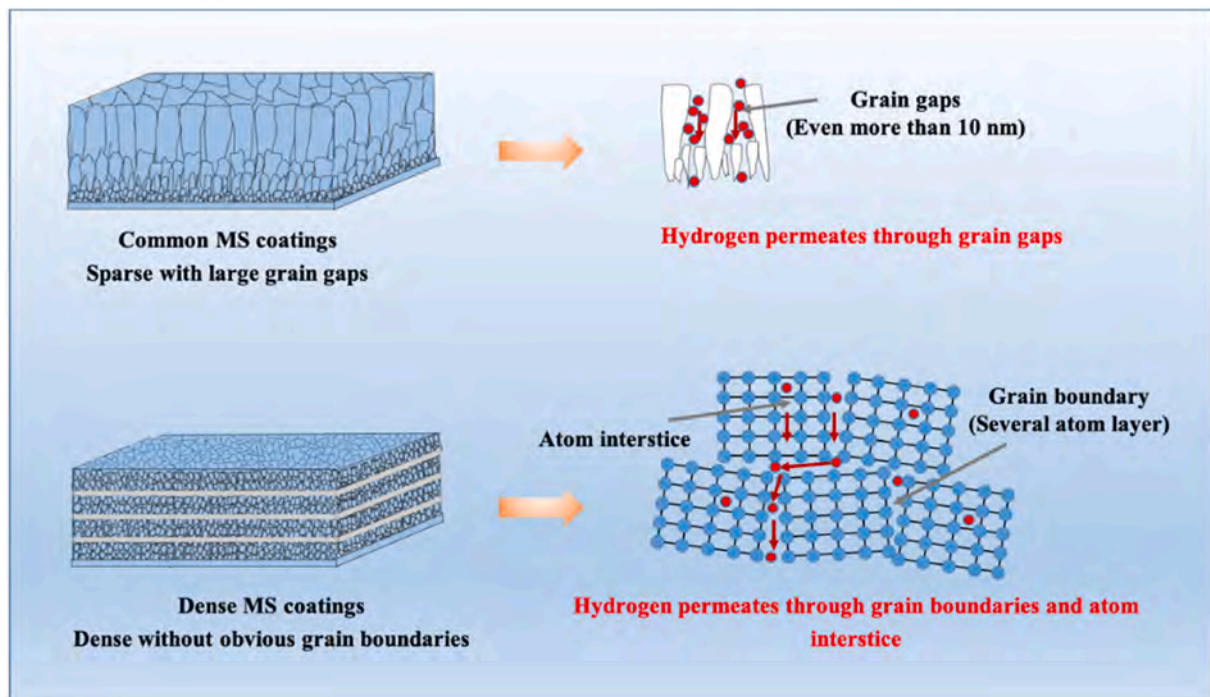**Fig. 10.** Fracture morphologies of the samples.

Fig. 11. Hydrogen resistance mechanism of the typical MS coatings and dense coatings.

Chu: Supervision.

Declaration of competing interest

The authors declare that they have no known competing financial interests or personal relationships that could have appeared to influence the work reported in this paper.

Acknowledgements

References

[1] O.J. Abe, A. Popoola, E. Ajenifuja, et al., Hydrogen energy, economy and storage: review and recommendation, Int. J. Hydrog. Energy 44 (2019) 15072–15086, https://doi.org/10.1016/j.ijhydene.2019.04.068.

[2] M. Dadfarnia, A. Nagao, S. Wang, et al., Recent advances on hydrogen embrittlement of structural materials, Int. J. Fract. 196 (2015) 223–243, https://doi.org/10.1007/s10704-015-0068-4.

[3] Z.Z. Zhang, X.R. Zuo, Y.Y. Hu, et al., Microstructure and mechanical properties analysis of X70 pipeline steel with polygonal ferrite plus granular bainite

microstructure, Appl. Mech. Mater. 161 (2012) 67–71, https://doi.org/10.4028/www.scientific.net/AMM.161.67.

[4] D.S. Bae, C.E. Sung, H.J. Bang, Effect of highly pressurized hydrogen gas charging on the hydrogen embrittlement of API X70 steel, Met. Mater. Int. 20 (2014) 653–658, https://doi.org/10.1007/s12540-014-4010-5.

[5] J.D. Fowler, D. Chandra, T.S. Elleman, et al., Tritium diffusion in Al2O3 and BeO, J. Am. Ceram. Soc. 60 (1977) 155–161, https://doi.org/10.1111/j.1151-2916.1977.tb15493.x.

[6] B.S. Yilbas, A. Coban, R. Kahraman, et al., Hydrogen embrittlement of Ti-6Al-4V alloy with surface modification by TiN coating, Int. J. Hydrog. Energy 23 (1998) 483–489, https://doi.org/10.1016/S0360-3199(97)00087-6.

[7] R. Checchetto, M. Bonelli, L.M. Gratton, et al., Analysis of the hydrogen permeation properties of TiN-TiC bilayers deposited on martensitic stainless steel, Surf. Coat. Technol. 83 (1996) 40–44, https://doi.org/10.1016/0257-8972(96)02851-4.

[8] S.C. Lee, W.Y. Ho, C.C. Huang, et al., Hydrogen embrittlement and fracture toughness of a titanium alloy with surface modification by hard coatings, J. Mater. Eng. Perform. 5 (1996) 64–70, https://doi.org/10.1007/BF02647271.

[9] S. Li, D. He, X. Liu, et al., Deuterium permeation of amorphous alumina coating on 316L prepared by MOCVD, J. Nucl. Mater. 420 (2012) 405–408, https://doi.org/10.1016/j.jnucmat.2011.10.040.

[10] V. Nemanič, P.J. McGuiness, N. Daneu, et al., Hydrogen permeation through silicon nitride films, J. Alloys Compd. 539 (2012) 184–189, https://doi.org/10.1016/j.jallcom.2012.05.110.

[11] J. Matějíček, J. Veverka, V. Nemani, et al., Characterization of less common nitrides as potential permeation barriers, Fusion Eng. Des. 139 (2019) 74–80, https://doi.org/10.1016/j.fusengdes.2018.12.056.

[12] G. Bruer, B. Szyszka, M. Verghl, et al., Magnetron sputtering – milestones of 30 years, Vacuum 84 (2010) 1354–1359, https://doi.org/10.1016/j.vacuum.2009.12.014.

[13] R. Kukla, Magnetron sputtering on large scale substrates: an overview on the state of the art, Surf. Coat. Technol. 93 (1997) 1–6, https://doi.org/10.1016/S0257-8972(97)00018-2.

[14] L.L. Liu, W. Tang, L. Zhou, et al., Comparative study of TiAlN coatings deposited by different high-ionization physical vapor deposition techniques, Ceram. Int. 46 (2020) 10814–10819, https://doi.org/10.1016/j.ceramint.2020.01.092.

[15] P. Panjan, M. Ekada, M. Panjan, et al., Surface density of growth defects in different PVD hard coatings prepared by sputtering, Vacuum 86 (2012) 794–798, https://doi.org/10.1016/j.vacuum.2011.07.013.

[16] Q. Li, J. Wang, Q.Y. Xiang, et al., Study on influence factors of permeation reduction factor of Al2O3 -hydrogen isotopes permeation barriers, Int. J. Hydrog. Energy 41 (2016) 4326–4331, https://doi.org/10.1016/j.ijhydene.2016.01.018.

[17] A. Perujo, K.S. Forcey, Tritium permeation barriers for fusion technology, Fusion Eng. Des. 28 (1995) 252–257, https://doi.org/10.1016/0920-3796(95)90045-4.

[18] G.W. Hollenberg, E.P. Simonen, G. Kalinen, et al., Tritium/hydrogen barrier development, Fusion Eng. Des. 28 (1995) 190–208, https://doi.org/10.1016/0920-3796(95)90039-X.

[19] A.A. Solovyev, V.O. Oskirko, V.A. Semenov, et al., Comparative study of Cu films prepared by DC, high-power pulsed and burst magnetron sputtering, J. Electron. Mater. 45 (2016) 1–9, https://doi.org/10.1007/s11664-016-4582-6.

[20] Z.W. Liu, C.Y. Hsu, M.C. Wu, et al., The effect of substrate temperature on the properties of (AlCrNbSiTiV)N films deposited by HIPIMS, Int. J. Adv. Manuf. Tech. 104 (2019) 4509–4516, https://doi.org/10.1007/s00170-019-04251-7.

[21] D. Bhaduri, A. Ghosh, S. Gangopadhyay, et al., Effect of target frequency, bias voltage and bias frequency on microstructure and mechanical properties of pulsed DC CFUBM sputtered TiN coating, Surf. Coat. Technol. 204 (2010) 3684–3697, https://doi.org/10.1016/j.surfcoat.2010.04.047.

[22] J.A. Thornton, Influence of apparatus geometry and deposition conditions on the structure and topography of thick sputtered coatings, J. Vac. Sci. Technol. 11 (1974) 666–670, https://doi.org/10.1116/1.1312732.

[23] K. Rajan, R. Roy, J. Trogolo, et al., Low energy ion beam assisted grain size evolution in thin film deposition, J. Electron. Mater. 26 (1997) 1270–1273, https://doi.org/10.1007/s11664-997-0068-x.

[24] I. Petrov, P.B. Barna, L. Hultman, et al., Microstructural evolution during film growth, J. Vac. Sci. Technol. A 21 (2003) S117–S128, https://doi.org/10.1116/1.1601610.

[25] B. Peng, Y.X. Xu, W.D. Jian, Influence of preliminary metal-ion etching on the topography and mechanical behavior of TiAlN coatings on cemented carbides, Surf. Coat. Technol. 432 (2022), 128040, https://doi.org/10.1016/j.surfcoat.2021.128040.

[26] L.L. Liu, Q.D. Ruan, Z.Z. Wu, et al., Hard and tough CrN coatings strengthened by high-density distorted coherent grain boundaries, J. Alloys Compd. 894 (2022), 162139, https://doi.org/10.1016/j.jallcom.2021.162139.

[27] M.A.V. Devanathan, Z. Stachurski, The adsorption and diffusion of electrolytic hydrogen in palladium[J], Proc. R. Soc. A-Math. Phys. Eng. Sci. 1962 (270) (1962) 90–102, https://doi.org/10.1098/rspa.1962.0205.

[28] Y.F. Cheng, Analysis of electrochemical hydrogen permeation through X-65 pipeline steel and its implications on pipeline stress corrosion cracking, Int. J. Hydrog. Energy 32 (2007) 1269–1276, https://doi.org/10.1016/j.ijhydene.2006.07.018.

[29] A. Turnbull, M. Maria, N.D. Thomas, The effect of H2S concentration and pH on hydrogen permeation in AISI 410 stainless steel in 5% NaCl, Corros. Sci. 29 (1989) 89–104, https://doi.org/10.1016/0010-938X(89)90082-6.

[30] P. Zhou, W. Li, X. Zhu, et al., Graphene containing composite coatings as a protective coatings against hydrogen embrittlement in quenching & partitioning high strength steel, J. Electrochem. Soc. 163 (2016) D160–D166, https://doi.org/10.1149/2.0551605jes.

[31] E. Martinez-Paneda, Z.D. Harris, S. Fuentes-Alonso, et al., On the suitability of slow strain rate tensile testing for assessing hydrogen embrittlement susceptibility, Corros. Sci. 163 (2020), 108291, https://doi.org/10.1016/j.corsci.2019.108291.

[32] B.E. Warren, X-ray Diffraction, Courier Corporation, 1969.

[33] S.H. Ahn, Y.S. Choi, J.G. Kim, et al., A study on corrosion resistance characteristics of PVD Cr-N coated steels by electrochemical method, Surf. Coat. Technol. 150 (2002) 319–326, https://doi.org/10.1016/S0257-8972(01)01529-8.

[34] N.S. Mansoor, A. Fattah-Alhosseini, H. Elmkhah, et al., Electrochemical behavior of TiN, CrN and TiN/CrN nanostructured coatings on the nickel-chromium alloy used in dental fixed prosthesis, J. Asian Ceram. Soc. 8 (2020) 1–17, https://doi.org/10.1080/21870764.2020.1776915.